

Basic Duchamp Testing

Tobias Westmeier

1 February 2011

1 Introduction

This document presents and discusses the results of basic source finding tests with Duchamp, the standard ASKAP source finder. For this purpose we generated a set of model sources that are spatially unresolved and possess a simple Gaussian spectral line profile. The main aim of the tests was to study the performance of Duchamp on sources of different signal-to-noise ratio and assess the accuracy of Duchamp's source parametrisation.

2 Model data

2.1 Two-dimensional images

In order to create a model data set for testing Duchamp, the MIRIAD task UVGEN was employed to generate visibility data of Gaussian noise with ASKAP characteristics and parameters similar to those anticipated for the WALLABY survey. The model parameters are summarised in Table 1.

The visibility data were Fourier-transformed using MIRIAD's task INVERT to generate a single-plane noise image of 600×600 pixels with characteristics similar to WALLABY (again, see Table 1 for details). The RMS noise level in this image is $\sigma = 1.95$ mJy which is only slightly higher than the 1.6 mJy expected for WALLABY.

In order to generate images of point sources the MIRIAD task IMGGEN was used to create 1024 images each of which has a size of 31×31 pixels and contains a single point source in the centre. Each source was randomly assigned a flux in the range of 1 to 20σ , resulting in an average of about 54 sources per 1σ interval.

Each of the 1024 images was convolved with the beam model produced by INVERT. Next, a random portion of 31×31 pixels of the original noise image was selected and added to each convolved image to create the final images used for testing Duchamp. To facilitate correct integrated flux measurements, we included information on the synthesised beam in the header of each image. The entire procedure is outlined in Fig. 1. Example images of three sources at peak flux levels of 3σ , 5σ , and 10σ are presented in Fig. 2.

2.2 Three-dimensional cubes

In addition to the two dimensional images introduced above we generated another 1024 three-dimensional data cubes of point sources with a spectral line component. The parameters are almost identical to those of the two-dimensional images. Again, we created point

Parameter (visibility)	Value	Unit
Number of antennas	36	
System temperature	50	K
Declination	-45°	
Total integration time	8	h
Hour angle range	± 4	h
Cycle time	5	s
Stokes parameters	I	
Number of channels	1 / 31	
Frequency	1.42	GHz
Channel width	18.31	kHz
	3.86	km s^{-1}
Parameter (image)	Value	Unit
Final image size	31×31	px
Field diameter	$5'$	
Pixel size	$10''$	
Robustness	0	
Gaussian uv taper	7.28	$\text{k}\lambda$
	1.54	km
RMS noise	1.95	mJy
Synthesised beam		
major axis	$27''1$	
minor axis	$26''7$	
position angle	$87^\circ9$	

Table 1: Summary of the parameters used to generate the visibility data set and noise image for the tests described in this document.

sources with peak flux levels between 1 and 20σ . In addition, we generated 31 spectral channels (instead of just one) and fitted each source with a Gaussian line profile. Line widths (FWHM) range from 0.1 to 10 spectral channels, equivalent to approximately 0.4 to 38.6 km s^{-1} , resulting in a density of about 27 sources per 1 km s^{-1} line width interval. All other parameters are identical to those of the two-dimensional models as discussed before and shown in Table 1.

3 Running Duchamp

Next, we ran Duchamp (version 1.1.8) on both the two-dimensional images and three-dimensional data cubes. In both cases, a 1.5σ flux threshold was employed, equivalent to 2.9 mJy. In addition, we made use of Duchamp’s “à trous” wavelet reconstruction. For the two-dimensional models we used a two-dimensional reconstruction with a minimum scale of 2 and a flux threshold of 4σ for wavelet components to be included in the reconstructed cube. In addition, we required sources to cover a minimum of 10 contiguous pixels above the detection threshold.

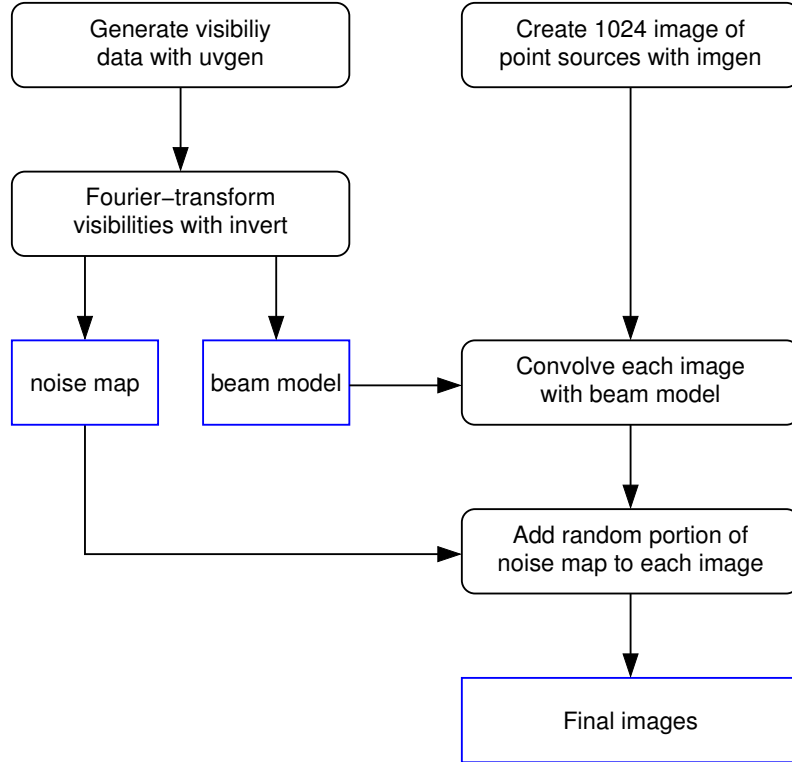


Figure 1: Outline of the procedure used to create the model images.

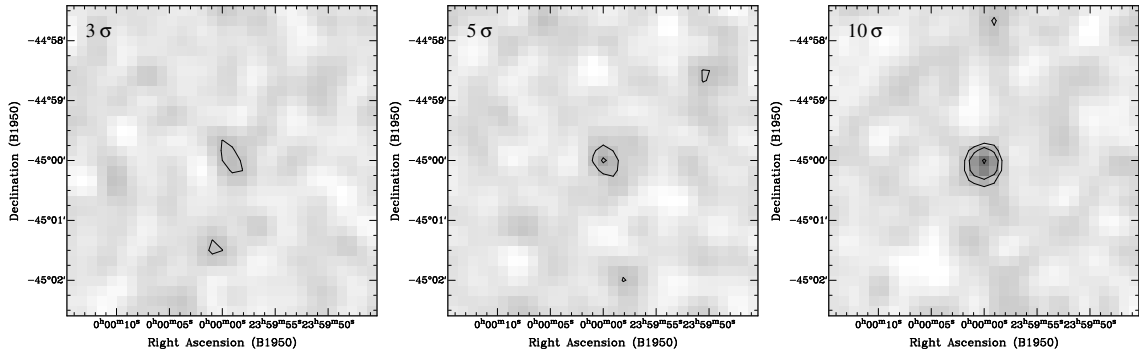


Figure 2: Two-dimensional images of three sources with peak flux levels of approximately 3σ , 5σ , and 10σ . The contour levels are 3σ , 5σ , and 10σ .

For the three-dimensional model we employed a full three-dimensional wavelet reconstruction with a minimum scale of 2 and a flux threshold of 3σ for wavelet components to be included in the reconstructed cube. In addition, we required sources to cover a minimum of 5 contiguous pixels and 3 contiguous channels above the detection threshold.

The output parameter files generated by Duchamp (1024 each for the two-dimensional and three-dimensional models) were concatenated, and those source entries whose positions were within ± 1 pixel of the nominal source position were considered as genuine sources and

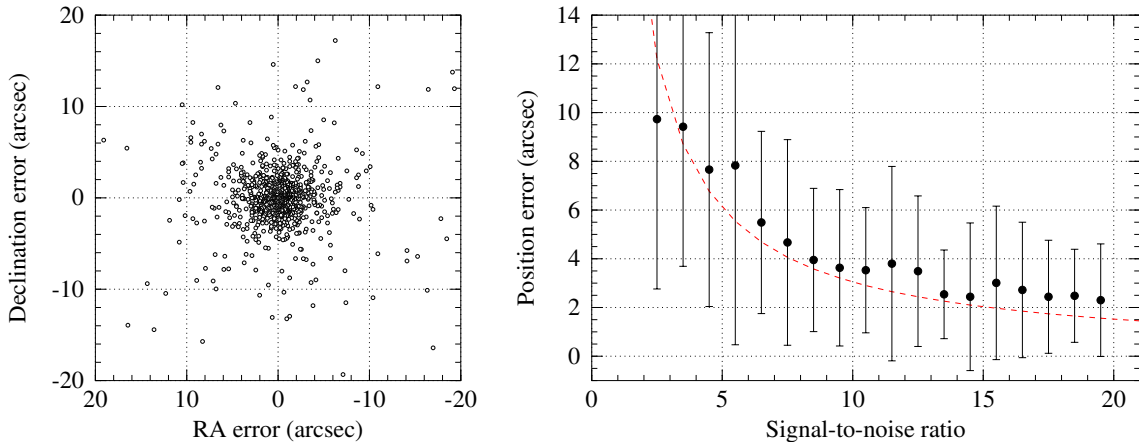


Figure 3: *Left-hand panel:* Position error of the two-dimensional model sources in right ascension and declination. *Right-hand panel:* Mean position error (black data points) and corresponding standard deviation (error bars) as a function of true signal-to-noise ratio in 1σ bins. The red, dashed curve shows the theoretical error expected from the fitting of two-dimensional Gaussian functions to the image.

selected for further processing and analysis. The results of this analysis will be presented and discussed in the following sections.

4 Results for two-dimensional images

4.1 Source position

The position errors of all 1024 model sources are plotted in the left-hand panel of Fig. 3. Apparently, Duchamp does an excellent job in determining accurate positions of point sources in two-dimensional images. The positions derived by Duchamp are perfectly centred on the nominal position of the model sources with a mean deviation of $-0''.1 \pm 4''.1$ in right ascension and $0''.0 \pm 3''.9$ in declination.

The right-hand panel of Fig. 3 shows the mean position error (in terms of angular separation from the nominal position) as a function of peak signal-to-noise ratio, F_{peak}/σ , with a binning of 1σ . For sources with high signal-to-noise ratio the position error is very small, approaching $2''$ at $F_{\text{peak}} \approx 20\sigma$. For sources with low signal-to-noise ratio there is a sharp increase in position error with values approaching $10''$ below $F_{\text{peak}} \approx 3\sigma$. The former corresponds to only 7%, the latter to approximately 37% of the FWHM of the synthesised telescope beam.

The red, dashed line in the right-hand panel of Fig. 3 shows for comparison the theoretical error expected for the fitting of two-dimensional Gaussian functions to the image,

$$\Delta r = \frac{2}{\sqrt{\pi}} \times \frac{\vartheta\sigma}{F_{\text{peak}}} \quad (1)$$

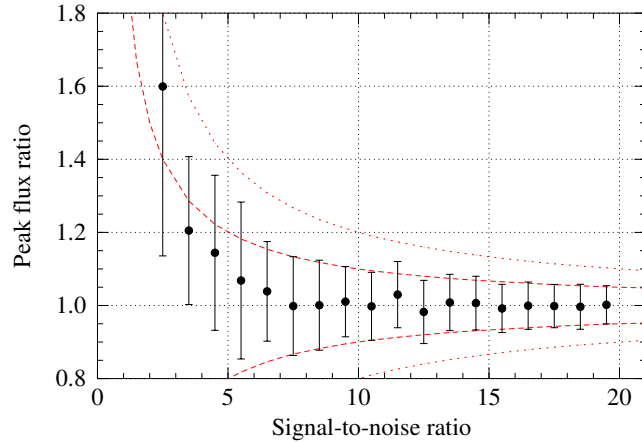


Figure 4: Ratio of recovered versus true peak flux of the two-dimensional model sources (black data points) and corresponding standard deviation (error bars) as a function of true signal-to-noise ratio in 1σ bins. The red, dashed and dotted curves show the 1σ and 2σ envelopes, respectively.

(adapted from Condon 1997),¹ where ϑ is the width of the Gaussian and equal to the FWHM of the synthesised beam in our case. The measured position error, although derived by Duchamp from the intensity-weighted centroid instead of a Gaussian fit, nicely follows the inverse signal-to-noise ratio relation of the theoretical curve.

4.2 Peak flux

The ratio of recovered versus original peak flux of the model sources as a function of signal-to-noise ratio is plotted in Fig. 4. In theory we would expect the mean ratio to be exactly 1, assuming that the errors caused by noise peaks are symmetric. As seen in Fig. 4, this is indeed the case for high peak fluxes of $F_{\text{peak}} \gtrsim 7\sigma$. At the same time, the scatter gradually increasing towards lower fluxes as the contribution of the constant RMS noise to the relative flux error increases.

Below about 5σ there is a sharp increase in the peak flux ratio, indicating that the peak fluxes recovered by Duchamp are systematically too large. This is not unexpected, because sources at low signal-to-noise ratios have a higher probability of being detected when they get boosted above the detection threshold by positive noise peaks, whereas the coincidence of a negative noise peak with the position of a weak source would likely result in its remaining undetected.

To quantify this effect, we can take a look at the theoretical peak flux error at the 1σ and 2σ levels, which are shown in Fig. 4 as the dashed and dotted red lines, respectively. For high signal-to-noise ratios the measured fluxes and standard deviations exactly match the theoretical expectation and perfectly coincide with the 1σ envelope. For low fluxes

¹Note that an additional factor of $\sqrt{2}$ was included to account for the maximum possible factor between the error in radius, r , as compared to the separate errors in either x or y , assuming that $r = \sqrt{x^2 + y^2}$. Furthermore, the implicit assumption is made that neighbouring pixels of the image are uncorrelated, whereas pixels in interferometric images are usually partly correlated.

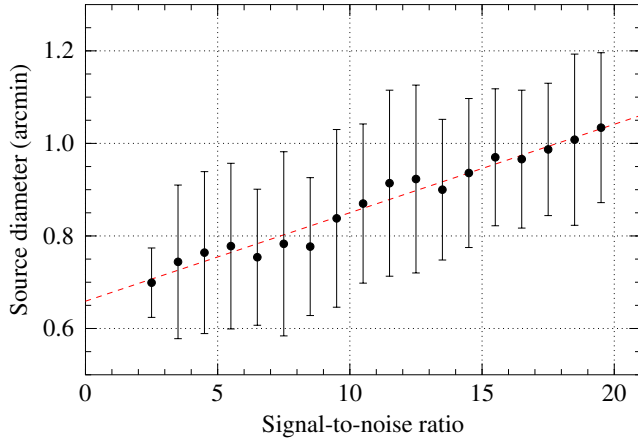


Figure 5: Mean diameter of the two-dimensional sources detected by Duchamp (black data points) and corresponding standard deviation (error bars) as a function of true signal-to-noise ratio in 1σ bins. The red, dashed line is the result of a linear fit to the data points.

the peak flux ratio approaches the upper envelope, indicating that detectability of sources below about 5σ is largely determined by chance coincidences with positive noise signals, while sources that coincide with negative noise signals will mostly go undetected.

4.3 Source diameter

The mean angular diameter of sources detected by Duchamp as a function of signal-to-noise ratio is plotted in Fig. 5. Duchamp provides separate diameters in right ascension and declination, and the values shown in Fig. 5 were derived by calculating the mean of the two, $w = 0.5 \times (w_{\text{RA}} + w_{\text{Dec}})$. For comparison, the red, dashed line shows the result of a linear fit to the data points yielding

$$\frac{w}{\text{arcmin}} = 0.0191 \frac{F_{\text{peak}}}{\sigma} + 0.659. \quad (2)$$

Despite all sources being unresolved, Duchamp does provide a value for the angular diameter, and apparently there is a perfectly linear relationship between that angular diameter and the peak flux of a source, bright sources having a larger diameter.

This unexpected behaviour can be explained when looking into how Duchamp actually determines source sizes. In fact, the individual size values provided by Duchamp only take discrete values that are multiples of $5''$, half the size of a pixel in the image. This suggests that the software somehow simply counts the number of pixels across each detection to derive the angular diameter. The linear relation in Fig. 5 is now easy to understand, because bright sources will be larger in the sense of generating more pixels above the detection threshold of Duchamp. Consequently, the size information provided by Duchamp for compact or unresolved sources is not meaningful because the method used by the software for calculating source sizes will only be appropriate for very extended sources. Hence, source diameter information produced by Duchamp should generally be approached with great caution.

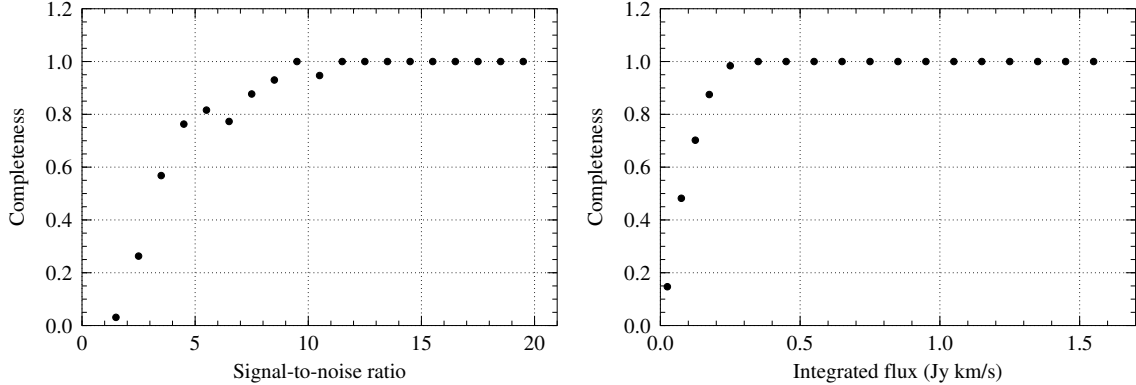


Figure 6: *Left-hand panel:* Completeness of the three-dimensional model sources as a function of true peak signal-to-noise ratio in bins of 1σ . *Right-hand panel:* Same, but as a function of true integrated flux in bins of 0.1 Jy km s^{-1} .

5 Results for three-dimensional data cubes

5.1 Completeness

Completeness, defined as the number of detections divided by the total number of sources, as a function of peak signal-to-noise ratio is plotted in the left-hand panel of Fig. 6. The detection list produced by Duchamp is complete down to a peak flux level of $F_{\text{peak}} \approx 10\sigma$, but below that level completeness decreases to below 50% at about 3σ . The completeness curve is “better behaved” when plotted against integrated flux instead of peak flux (right-hand panel of Fig. 6). The 100% completeness level is reached at $F_{\text{int}} \approx 0.3 \text{ Jy km s}^{-1}$, and below that flux level there is a sharp drop in completeness.

The reason for the much sharper decline as a function of integrated flux is that Duchamp is sensitive to a certain level of integrated (as opposed to peak) signal-to-noise ratio, as is demonstrated in the left-hand panel of Fig. 7 where the FWHM of the spectral line is plotted against peak signal-to-noise ratio for all detected (black) and undetected (red) sources. There is a clear degeneracy between faint sources with broad lines and bright sources with narrow lines, both of which might end up having the same integrated flux and thus remain undetected.

The completeness analysis as a function of integrated flux, as shown in the right-hand panel of Fig. 6, allows us to assess the HI mass sensitivity of surveys like WALLABY and DINGO. Using the following conversion between integrated flux and HI mass,

$$\frac{M_{\text{HI}}}{M_{\odot}} = 0.236 \frac{F_{\text{int}}}{\text{Jy km s}^{-1}} \left(\frac{d}{\text{kpc}} \right)^2, \quad (3)$$

we can calculate the expected HI mass sensitivity as a function of distance, d , for varying levels of completeness.

This is shown in the right-hand panel of Fig. 7 where the HI mass sensitivities as a function of distance for levels of 100% and 50% completeness are plotted as the solid blue and red lines, respectively. The former is equivalent to $0.25 \text{ Jy km s}^{-1}$ and the latter to $0.075 \text{ Jy km s}^{-1}$. The 100% completeness level translates into mass sensitivities of 10^5 ,

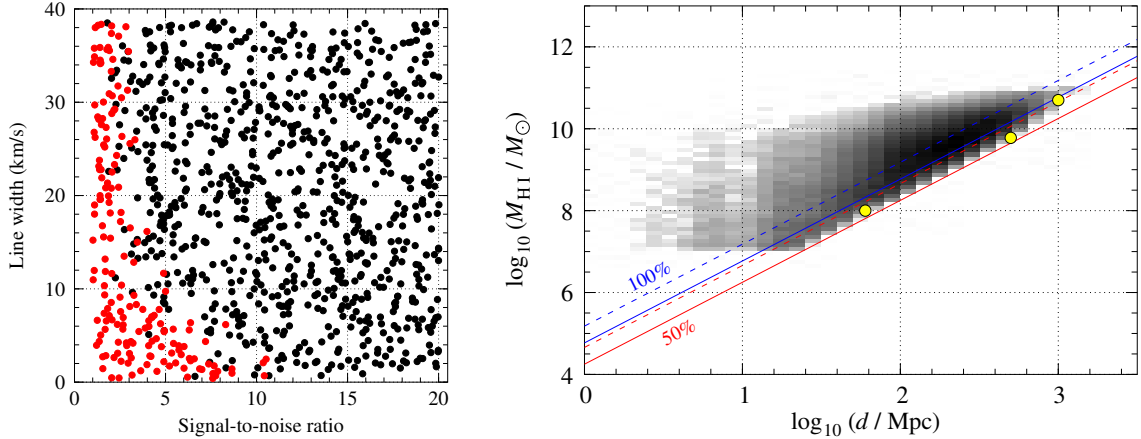


Figure 7: *Left-hand panel:* True FWHM of the spectral line versus true peak signal-to-noise ratio for all detected (black) and undetected (red) three-dimensional model sources. *Right-hand panel:* 100% (blue lines) and 50% (red lines) completeness limits as calculated from our completeness analysis in the right-hand panel of Fig. 6. The solid lines show the original limits derived from Duchamp’s output while the dashed lines have been corrected for different noise levels (1.6 vs. 1.95 mJy) and galaxy line widths (200 vs. 20 km s^{-1}) of WALLABY as compared to our input models. The greyscale image shows the number of expected detections (on a logarithmic scale) based on previous, internal WALLABY completeness simulations, and the yellow data points show three sensitivity estimates from the WALLABY proposal for comparison.

10^7 , 10^9 , and $10^{11} M_{\odot}$ at distances of 1, 10, 100, and 1000 Mpc, respectively. The mass limits at 50% completeness are by a factor of 4.7 lower.

To compare these sensitivities with the expectations for WALLABY, the greyscale image in the right-hand panel of Fig. 7 shows the number of expected detections (using a logarithmic scale and bins of 0.1×0.1 dex) based on previous, internal simulations of WALLABY completeness as a function of distance and HI mass. These simulations assumed a somewhat lower RMS noise level compared to our model cubes (1.6 vs. 1.95 mJy) and typically larger galaxy line widths (200 vs. 20 km s^{-1}). Both effects combined result in our completeness lines being shifted upwards by a factor of $\sqrt{200/20} \times (1.6/1.95) \approx 2.6$. The corrected mass sensitivity levels have been plotted as the dashed lines in Fig. 7 and are in excellent agreement with the grayscale image from the simulation, suggesting that Duchamp can reach the sensitivity levels required for the aims of WALLABY.

The plot also includes three sensitivity estimates from the WALLABY proposal as the yellow data points. These correspond to $10^8 M_{\odot}$ at 60 Mpc, $6 \times 10^9 M_{\odot}$ at 500 Mpc, and $5 \times 10^{10} M_{\odot}$ at 1 Gpc. All three estimates are in good agreement with the results of the Duchamp source finding test and lie near the corrected 50% completeness level, confirming that Duchamp can in principal reach the sensitivity levels required for the success of WALLABY.

Fig. 8 shows a similar plot for the DINGO project based on earlier completeness simulations for the deep (left-hand panel) and ultra-deep (right-hand panel) surveys of DINGO. The dashed lines have again been corrected for differences in RMS noise and line

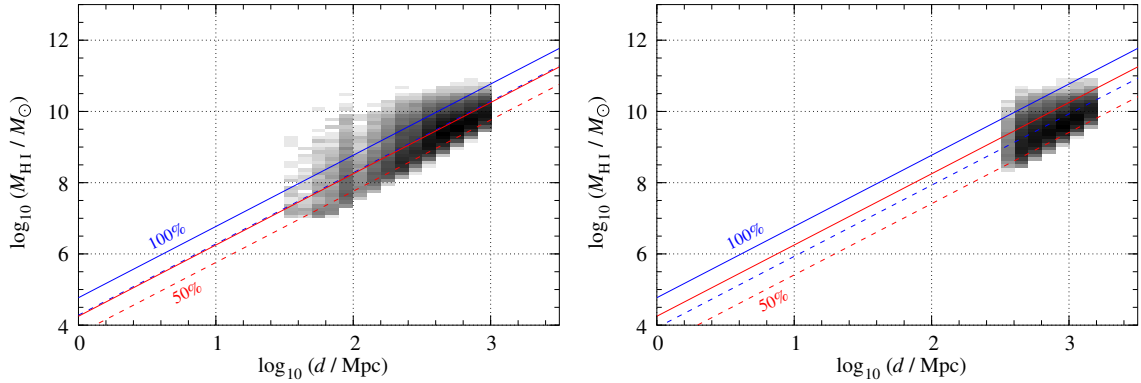


Figure 8: Same as in the right-hand panel of Fig. 7, but for the DINGO deep (*left-hand panel*) and ultra-deep (*right-hand panel*) surveys. The dashed lines have again been corrected, this time to match the parameters of DINGO.

width, this time using the expected DINGO noise levels of $200 \mu\text{Jy}$ (deep) and $90 \mu\text{Jy}$ (ultra-deep)² and assuming a typical H I line width of 200 km s^{-1} FWHM. Again, the outcome of the Duchamp testing appears to be roughly consistent with expectations from the DINGO completeness simulations, suggesting that Duchamp is capable of reaching the sensitivity limits required for the deep and ultra-deep parts of DINGO.

A few words of caution shall be raised at this point. First of all, the sources discussed here have a very simple structure (point sources with Gaussian spectral profiles). Real galaxies detected by WALLABY and DINGO will have a much more complex morphology which will influence the performance of Duchamp. Secondly, the positions and velocities of the sources discussed here were exactly known, and false detections could be discarded very efficiently due to their “wrong” positions and velocities. WALLABY and DINGO, however, will have to deal with a large number of false detections, and reliably discarding these based on their parameters will be a great challenge.

5.2 Source position

The position errors produced by Duchamp in the case of three-dimensional model sources are plotted in the left-hand panel of Fig. 9. As in the two-dimensional case, Duchamp does an excellent job in determining accurate source positions, with a mean position error of $0''.0 \pm 1''.6$ in right ascension and $0''.1 \pm 1''.5$ in declination. This is even more accurate than in the two-dimensional scenario, reflecting the higher effective signal-to-noise ratio due to the sources being extended in the frequency domain.

The mean position error (in terms of angular separation from the nominal source position) as a function of peak signal-to-noise ratio, in bins of 1σ , is shown in the right-hand panel of Fig. 9. For bright sources of $F_{\text{peak}} \approx 20\sigma$ the mean position error is approximately $1''$, increasing to about $5''$ for $F_{\text{peak}} \approx 3\sigma$. These numbers correspond to only about 4% and 19%, respectively, of the FWHM of the synthesised beam, an improvement of about a factor of 2 with respect to the two-dimensional case. This improvement is consistent with

²A velocity resolution and channel width of 3.86 km s^{-1} (18.3 kHz) was assumed in both cases.

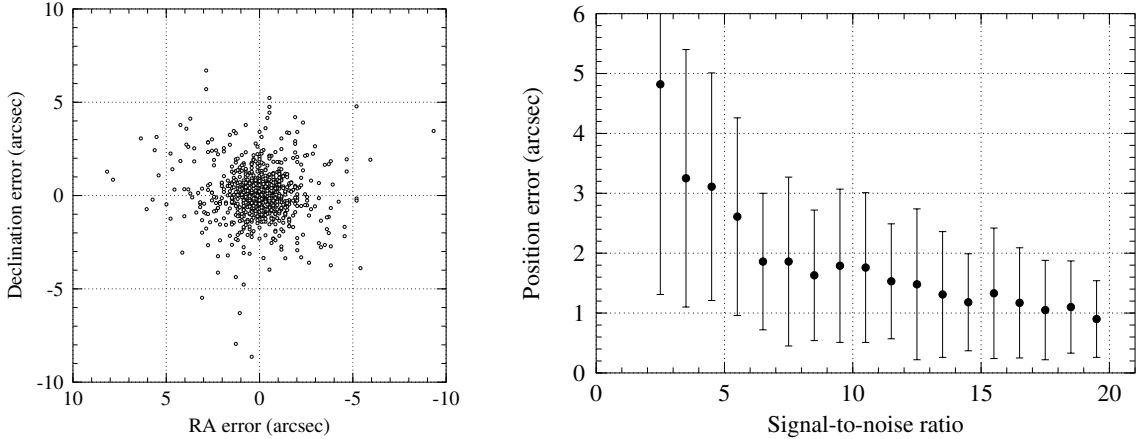


Figure 9: *Left-hand panel:* Position error of the three-dimensional model sources in right ascension and declination. *Right-hand panel:* Mean position error (black data points) and corresponding standard deviation (error bars) as a function of true peak signal-to-noise ratio in 1σ bins.

the expected increase in integrated signal-to-noise ratio of $\sqrt{5} \approx 2.2$ for a source with a line width of about 5 spectral channels, underlining Duchamp’s formidable position accuracy near the theoretical limit.

5.3 Radial velocity

An overall histogram of radial velocity errors produced by Duchamp is shown in the left-hand panel of Fig. 10. As expected, velocity errors have an approximately Gaussian distribution centred on zero. The mean velocity error of all sources is $0.0 \pm 1.7 \text{ km s}^{-1}$. The red, dashed curve in Fig. 10 shows the result of a Gaussian fit to the histogram. While the overall distribution of velocity errors follows the fitted Gaussian function, there are a few significant deviations, namely a somewhat higher and sharper peak in the centre (which is slightly shifted into the negative range) and conspicuous “wings” between 2 and 3 km s^{-1} (both positive and negative) where source counts are systematically too high with respect to the fit. The FWHM of the fitted Gaussian is $1.94 \pm 0.04 \text{ km s}^{-1}$, and the centroid is $-0.026 \pm 0.017 \text{ km s}^{-1}$ which deviates from zero by about 1.5σ , mainly reflecting the aforementioned negative offset of the peak of the histogram.

The standard deviation of the radial velocity error as a function of peak signal-to-noise ratio in 1σ bins is shown in the right-hand panel of Fig. 10. As expected, the standard deviation from the mean (which is basically zero) increases with decreasing peak flux. While for bright sources of $F_{\text{peak}} \approx 20\sigma$ the standard deviation is below 1 km s^{-1} , it increases to almost 6 km s^{-1} for faint sources near 3σ .

5.4 Line width

Fig. 11 shows the ratio of measured line width versus the true line width (FWHM of the original Gaussian model) as a function of peak signal-to-noise ratio in bins of 1σ . Duchamp determines three different kinds of line width: w_{50} is the width at 50% of the peak flux,

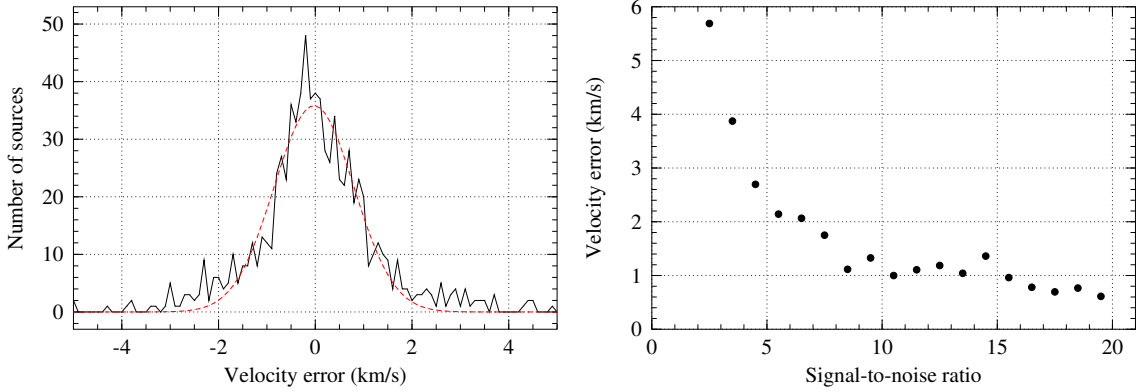


Figure 10: *Left-hand panel:* Histogram of radial velocity errors (black curve) of the three-dimensional model sources in bins of 0.1 km s^{-1} . The red, dashed curve is the result of a Gaussian fit to the histogram. *Right-hand panel:* Standard deviation of the velocity error of the sources as a function of peak true signal-to-noise ratio in bins of 1σ .

w_{20} is the width at 20% of the peak flux, and w_{vel} is the full line width of the source, i.e. the width across all channels with detected flux. For a Gaussian line, w_{50} is equivalent to the FWHM, and the ratio should therefore be 1. The relation between w_{20} and w_{50} in the case of a Gaussian line is given by the constant factor of

$$\frac{w_{20}}{w_{50}} = 1.53. \quad (4)$$

Finally, the relation between w_{vel} and w_{50} , again assuming a Gaussian function and a 1σ threshold for w_{vel} , is defined via

$$\frac{w_{\text{vel}}}{w_{50}} = \frac{\sqrt{-8 \ln(\sigma/F_{\text{peak}})}}{2.35} \quad (5)$$

where F_{peak}/σ is the signal-to-noise ratio. These theoretical relations are plotted in Fig. 11 as the dashed lines for w_{50} (black), w_{20} (red), and w_{vel} (blue).

Duchamp's measurement of w_{50} (black data points) is in excellent agreement with the expectation (black, dashed line) over a wide range of peak signal-to-noise ratios. Only for faint sources of $F_{\text{peak}} < 5\sigma$ the measured line widths are on average slightly smaller than the true widths, but by no more than about 10 to 15%.

In contrast, Duchamp's measurements of w_{20} and w_{vel} (red and blue data points, respectively) are clearly too large over most of the covered range of signal-to-noise ratios as compared to the theoretical expectations (red and blue dashed lines, respectively). Only for faint sources of $F_{\text{peak}} \lesssim 5\sigma$ do the measured values fall slightly below the theoretical ones. This result suggests that w_{50} is the most accurate measurement of line width provided by Duchamp and should be used instead of w_{20} and w_{vel} for the characterisation of astronomical sources. However, all line width measures, including w_{50} , systematically fall short of the true line width for faint sources below $F_{\text{peak}} \approx 5\sigma$.

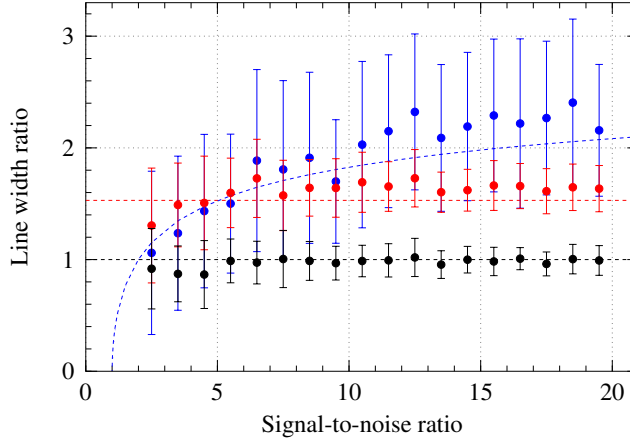


Figure 11: Ratio of measured versus true line width for three-dimensional model sources as a function of true peak signal-to-noise ratio in bins of 1σ . The black data points show w_{50} , the red data points w_{20} , and the blue data points w_{vel} , all of which have been divided by the original FWHM of the Gaussian line. The corresponding theoretical expectations are shown as the black, red, and blue dashed lines.

5.5 Peak flux

The ratio of recovered versus original peak flux of the sources is plotted in the left-hand panel of Fig. 12 as a function of peak signal-to-noise ratio in 1σ bins. The dashed and dotted red lines indicate the theoretical $\pm 1\sigma$ and $\pm 2\sigma$ envelopes, respectively. The right-hand panel shows the same figure, but as a function of integrated flux in bins of 0.1 Jy km s^{-1} . For bright sources of $F_{\text{peak}} \gtrsim 10\sigma$ Duchamp accurately recovers the peak flux of the sources, although there is the general tendency of measured peak fluxes being slightly too high on average. For fainter sources of $F_{\text{peak}} \lesssim 5\sigma$ there is a strong deviation, with fluxes being systematically overestimated by a significant factor. This is generally due to faint sources being more likely to be detected in the first place if their maximum coincides with a positive noise peak, whereas faint sources sitting on top of a negative noise peak will likely remain undetected, creating a strong bias in the measurement of peak fluxes.

Comparison with the two-dimensional case in Fig. 4 reveals a subtle difference in that the two-dimensional peak flux measurements are generally more accurate for bright sources, while the three-dimensional fluxes tend to be slightly overestimated even at higher signal-to-noise ratios. Duchamp determines the peak flux of a source by simply selecting the data element with the highest flux encountered. As mentioned before, this method is biased towards selecting data elements that have been affected by positive noise peaks. In three-dimensional data with broad spectral signals there is a higher probability of finding a positive noise signal in one of the channels near the peak of the line that increases the signal beyond the actual line peak. This is due to the object being well resolved in the spectral domain. Hence, peak fluxes in the three-dimensional data set generally get overestimated irrespective of source brightness (as long as the source is spectrally resolved), whereas this is not the case for the two-dimensional data set of point sources.

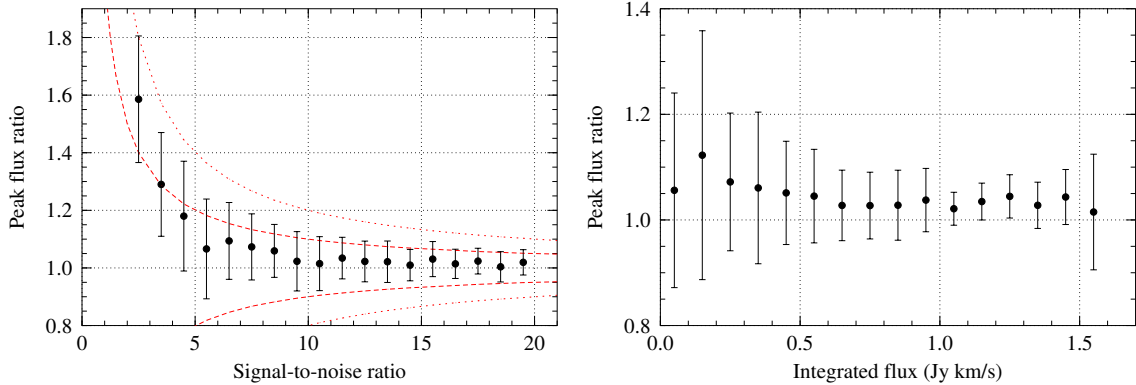


Figure 12: *Left-hand panel:* Ratio of measured versus true peak flux (black data points) and corresponding standard deviation (error bars) of the three-dimensional sources as a function of true peak signal-to-noise ratio in 1σ bins. The dashed and dotted red lines indicate the theoretical $\pm 1\sigma$ and $\pm 2\sigma$ envelopes, respectively. *Right-hand panel:* Same, but as a function of true integrated flux in bins of 0.1 Jy km s^{-1} .

5.6 Integrated flux

The ratio of measured versus true integrated flux of the sources as a function of peak signal-to-noise ratio in bins of 1σ is presented in the left-hand panel of Fig. 13. The right-hand panel shows the same figure, but as a function of integrated flux in bins of 0.1 Jy km s^{-1} . Apparently, Duchamp systematically underestimates the integrated flux of sources by a significant factor. Even for the brightest sources of $F_{\text{peak}} \approx 20\sigma$ only about 90% of the true flux is recovered by Duchamp, and that number drops to well below 50% for faint sources of $F_{\text{peak}} < 5\sigma$.

This issue is likely caused by the fact that Duchamp only considers pixels above the detection threshold when calculating the integrated flux. Pixels below the threshold, while contributing significantly to the overall flux of a source, are not included in the summation carried out by Duchamp, resulting in systematically underestimated integrated fluxes.

In order to study the expected decrease in the integrated flux measurement, let us assume a point source with Gaussian line profile,

$$F(v) = F_{\text{peak}} \exp\left(-\frac{v^2}{2s^2}\right), \quad (6)$$

with amplitude F_{peak} and dispersion s . The integrated flux measurement can then be considered as the integral under the Gaussian line across the frequency/velocity range of $\pm v_\sigma$ over which the flux of the line is above the spectral baseline RMS, thus

$$F_{\text{int}} = \int_{-v_\sigma}^{v_\sigma} F(v) dv = \sqrt{2\pi} s F_{\text{peak}} \operatorname{erf}\left(\frac{v_\sigma}{\sqrt{2} s}\right), \quad (7)$$

where $\operatorname{erf}(x)$ is the error function. The velocity range over which to integrate is given by

$$v_\sigma = \sqrt{-2s^2 \ln(\sigma/F_{\text{peak}})}, \quad (8)$$

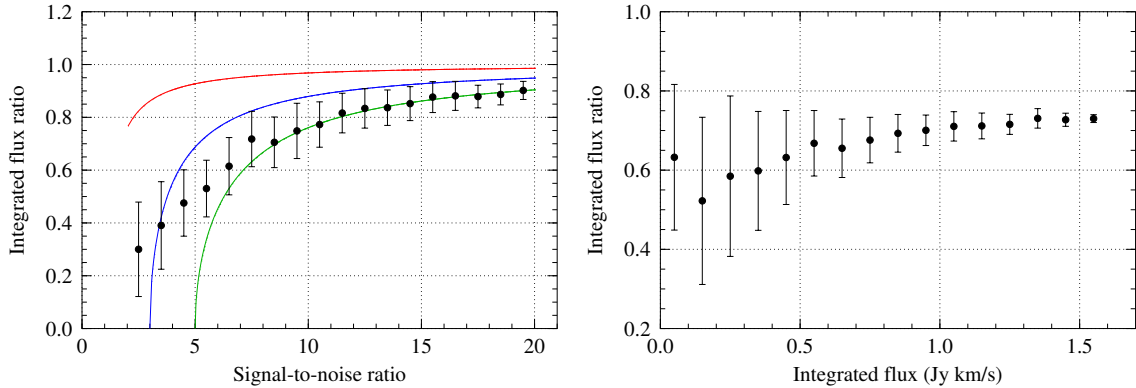


Figure 13: *Left-hand panel:* Ratio of measured versus true integrated flux (black data points) and corresponding standard deviation (error bars) of the three-dimensional sources as a function of true peak signal-to-noise ratio in bins of 1σ . The red, blue and green curves show the theoretical expectation for a 1σ , 3σ and 5σ flux cutoff, respectively. *Right-hand panel:* Same, but as a function of true integrated flux in bins of 0.1 Jy km s^{-1} .

where σ/F_{peak} is the inverse of the peak signal-to-noise ratio.

The resulting theoretical integrated flux measurement, normalised with respect to the total integrated flux and assuming a 1σ cutoff, is shown as the red curve on Fig. 13. The blue and green curves show the expected flux measurements for a 3σ and 5σ cutoff, respectively. Apparently, the integrated flux errors produced by Duchamp are significantly larger than what one would expect from a simple integration over the Gaussian line profile. Even for simple point sources with Gaussian line profiles Duchamp drastically underestimates the integrated flux. This is likely due to the fact that Duchamp measures the integrated flux of a source by integrating over all three dimensions instead of just the velocity axis, resulting in a slightly worse performance than the theoretical behaviour which assumed a point source. As a result of this, the integrated flux measurements provided by Duchamp would need to be corrected substantially to compensate for the systematic offset.

6 Summary and conclusions

In general, Duchamp does what it promises to do. It is able to reliably detect sources down to low signal-to-noise ratios and accurately determine their position and radial velocity within the theoretical limits. These are the most fundamental requirements for a source finder. Comparison of completeness and mass sensitivity levels with the outcome of previous WALLABY/DINGO simulations has shown that Duchamp can in principal reach the sensitivity required for the success of WALLABY and DINGO. However, when it comes to source parametrisation, the numbers produced by Duchamp are affected by several systematic errors. Most of these effects are not due to errors in the software itself, but a consequence of the methods and algorithms used for measuring source parameters.

The source diameter calculated by Duchamp for compact sources is meaningless and not related at all to the actual source size. Instead, the measured source diameter is purely

determined by a source's peak flux, because Duchamp seems to be calculating the spatial size by somehow counting the number of pixels across the source.

Spectral line widths determined by Duchamp are generally very accurate as far as the w_{50} parameter is concerned. The two other line width parameters calculated by Duchamp, w_{20} and w_{vel} , appear to be systematically overestimated over a wide range of signal-to-noise ratios and should not be used unless explicitly required in special and well-defined circumstances.

Peak fluxes are generally mildly overestimated by Duchamp for bright sources and strongly overestimated (on a relative scale) for faint sources below about 5σ . This is due to the fact that Duchamp determines the peak flux by simply selecting the value of the brightest pixel encountered. This method introduces a bias towards positive noise peaks sitting on top of the brightest region of a source, and hence peak fluxes measured by Duchamp will be systematically too high.

Finally, integrated fluxes are significantly and systematically underestimated by Duchamp, even for bright point sources. Furthermore, Duchamp's performance is somewhat worse than what is expected from simple theoretical considerations for point sources. This is likely caused by the fact that Duchamp simply adds the flux of all pixels above the threshold to determine the integrated flux. Hence, the raw integrated flux measurements currently provided by Duchamp are not useful and need to be corrected to compensate for the systematic offset. This issue is particularly sensitive as many scientific projects, including WALLABY and DINGO, rely on accurate flux measurements, e.g. to determine the HI mass function of galaxies.

In summary, Duchamp appears to be a successful source finder able to reliably detect sources and accurately determine their position and velocity while reaching the sensitivity levels required for the success of WALLABY and DINGO. In its current state, however, Duchamp is not particularly successful in parametrising the detected sources, and other, external algorithms for source parametrisation should be considered instead. It appears, however, that most, if not all, parametrisation issues are due to intrinsic deficiencies in the implemented algorithms themselves and not due to errors in their implementation, suggesting that most of the problems can in principle be solved by implementing more sophisticated parametrisation algorithms in Duchamp. Alternatively, corrections would have to be applied to all parameters derived by Duchamp.